

Non-adiabatic effects in exciton-mediated Raman scattering from first principles

Sven Reichardt^{1,2} and Ludger Wirtz²

¹*Department of Materials, University of Oxford, Parks Road, Oxford OX1 3PH, United Kingdom*

²*Physics and Materials Science Research Unit, University of Luxembourg, 1511 Luxembourg, Luxembourg*

We present an *ab initio* computational approach for the calculation of resonant, one-phonon Raman intensities from first principles that allows the combined inclusion of both excitonic and non-adiabatic effects. We apply our approach to two prototype layered materials: bulk hexagonal boron nitride and single-layer molybdenum disulfide (MoS₂). In case of the former, we demonstrate the emergence of strong quantum interference between excitonic resonances due to non-adiabatic effects and the suppression of higher excitonic resonances in the Raman intensity due to angular momentum conservation. In the case of MoS₂, we observe that non-adiabatic effects are suppressed by spin-orbit splitting, while we analyze the relative intensity of in- and out-of-plane Raman modes from the point of view of exciton-phonon coupling.

Raman spectroscopy is a versatile tool for the characterization of many materials and, in particular, 2D materials [1]. It allows the study of both vibrational and electronic properties. Among many other things, it serves to probe many-body [2] and non-adiabatic effects [3, 4] as well as excitonic ones [5, 6]. From a theoretical point of view, however, a general and comprehensive approach that captures both of these effects is missing so far. Regarding one-phonon Raman scattering, recent theoretical and computational efforts have focused either on a leading-order perturbation theory approach [7–13], which is able to capture non-adiabatic effects but not excitonic ones, or on a method based on the calculation of the change of the dielectric susceptibility with static atomic displacements along phonon modes [6, 14–18], which captures excitonic effects but is entirely adiabatic. As such, an approach that is able to capture both effects is highly desirable not only from a theoretical and conceptual point of view, but also in practice. This is especially true for systems with sizable phonon frequencies and strong excitonic effects or also for materials whose properties are *a priori* unknown.

In a recent work [19], we laid the groundwork for such a comprehensive theoretical description of Raman scattering from first principles that allows the inclusive description of both excitonic and non-adiabatic effects in one fully quantum mechanical theory. Here we now apply this general theory to the case of resonant, one-phonon Raman scattering. We present concrete expressions for the Raman intensity in terms of quantities that can be obtained by *ab initio* calculations on the level of density functional theory (DFT) and many-body perturbation theory (MBPT), i.e., within the *GW*-approximation for the quasi-particle band structure and solving the Bethe-Salpeter equation to include excitonic effects. We then apply it to two materials, bulk hexagonal boron nitride and monolayer molybdenum disulfide (MoS₂), which are known to feature strong excitonic effects in both absorption [20, 21] and Raman spectra [5, 22] due to their layered, two-dimensional structure. The modular structure of our method allows us to further analyze our numerical

results in detail and explain them in a physically intuitive way.

In the case of boron nitride our two main findings are (i) the suppression of some of the higher excitonic resonances in the Raman spectrum, contrary to their brightness in the optical absorption spectrum, and (ii) strong quantum interference between the first two excitonic resonances mediated by non-adiabatic effects, which leads to a strong redistribution of scattering weight from the first to the second exciton, something that cannot be captured in an adiabatic theory. In the case of monolayer MoS₂, we investigate (i) the difference in the coupling of the three main excitonic resonances to the in-plane and out-of-plane Raman modes and (ii) the effects of non-adiabaticity on the position of the main resonances.

We begin the discussion by giving a brief account of the theory and the concrete expressions we use in our numerical calculations. More details are provided in the Supplemental Material (SM) [23]. Our starting point is the expression of the Raman scattering rate in the quasi-particle approximation for the phonon and the dipole approximation for the incoming and outgoing photon which was derived in Ref. [19]:

$$\begin{aligned} \dot{P}_{\text{inel.}} \approx & \Gamma_{\text{kin.}}(\omega_L, \omega_D) \sum_{\lambda} \left| \tilde{\mathcal{M}}_{\mu\nu}^{\lambda}(\omega_L - \omega_D, \omega_D) \right|^2 \\ & \times \frac{Z_{\lambda}}{\pi} \frac{\Gamma_{\lambda}/2}{(\omega_L - \omega_D - \omega_{\lambda})^2 + (\Gamma_{\lambda}/2)^2}, \end{aligned} \quad (1)$$

where

$$\begin{aligned} \tilde{\mathcal{M}}_{\mu\nu}^{\lambda}(\omega', \omega) \equiv & \int_{-\infty}^{+\infty} dt e^{i\omega t} \int_{-\infty}^{+\infty} dt' e^{i\omega' t'} \\ & \times (-i) \langle 0 | \mathcal{T} \left[\hat{F}_{\lambda}(t') \hat{J}_{\nu}(t) \hat{J}_{\mu}^{\dagger}(0) \right] | 0 \rangle_{\text{connect.}} \end{aligned} \quad (2)$$

is the *reduced matrix element*, defined in terms of the *fully connected part* of the electronic force-current-current correlation function. The quantities appearing in the latter are the phonon eigenmode-projected electronic force operator $\hat{F}_{\lambda} \equiv \sum_I \mathbf{v}_I^{\lambda} \cdot \int d^3r \hat{\psi}^{\dagger}(\mathbf{r}) \hat{\psi}(\mathbf{r}) \partial V_{\text{lat}}(\mathbf{r}) / \partial (\mathbf{R}_I) |_{\{\mathbf{R}_I^{(0)}\}}$

and the light polarization-projected electronic current density operators in the dipole approximation $\hat{J}_\mu \equiv (-e/m)\epsilon_\mu^* \cdot \int d^3r \hat{\psi}^\dagger(\mathbf{r})(-i\nabla)\hat{\psi}(\mathbf{r})$. Here, all time-dependent operators are understood to be in the Heisenberg picture with respect to the full Hamiltonian of the matter system, whose ground state is denoted by $|0\rangle$. The vectors \mathbf{v}_I^λ and ϵ_μ denote the displacement vector of atom I according to a zero-momentum phonon mode λ with frequency ω_λ and the light polarization vector labeled by μ (ν) for the incoming (outgoing) photon, respectively. Further, $V_{\text{lat}}(\mathbf{r})$ denotes a fixed lattice potential of nuclei with equilibrium configuration $\{\mathbf{R}_I^{(0)}\}$ and $\hat{\psi}(\mathbf{r})$ is the electron field operator, with $(-e)$ and m being the charge and mass of an electron, respectively. Finally $\Gamma_{\text{kin.}}(\omega_L, \omega_D) \propto \omega_L \omega_D$ is a kinetic factor, which depends on the frequency ω_L (ω_D) of the incoming (outgoing) light and which was defined in Eq. (31) of Ref. [19].

The challenge in making the reduced matrix element of Eq. (2) accessible to a numerical computation lies in the complexity of the three-particle correlation function appearing as part of the force-current-current correlation function. In order to find an approximation for it that still captures excitonic and non-adiabatic effects, we treat both the electron-electron and the electron-phonon interaction in perturbation theory and carry out a diagrammatic analysis. This allows us to systematically truncate the perturbation series in a way that captures the relevant physics, but can still be evaluated in a way suitable for a numerical calculation. The approximation for the reduced matrix element that we use in this work is shown in Fig. 1 and will be referred to as *ladder-like approximation* (LLA) in the following. The main advantage of the LLA is that it allows a modular evaluation of the reduced matrix element. The diagrammatic series for the exact vertices can be summed in closed-form by making use of the Bethe-Salpeter equation, while the part of the diagram that connects the three vertices is simply given by the *independent-particle* (IP) three-particle correlation function. This approximation neglects terms of the perturbation series that include the variational derivative of the two-particle interaction kernel with respect to the one-particle Green's function [24]. This kind of approximation is typically also successfully used in state-of-the-art approaches for the computation of optical absorption spectra [25, 26], where it corresponds to neglecting the variational derivative of the screened inter-electron Coulomb interaction with respect to the one-particle Green's function.

On top of the LLA, we employ three further approximations to make the computations practically feasible: (i) We approximate the two-particle interaction kernel in the electron-photon vertex by a kernel consisting of the sum of a statically screened Coulomb interaction to mediate the electron-hole interaction and a repulsive bare exchange interaction. This approximation is routinely

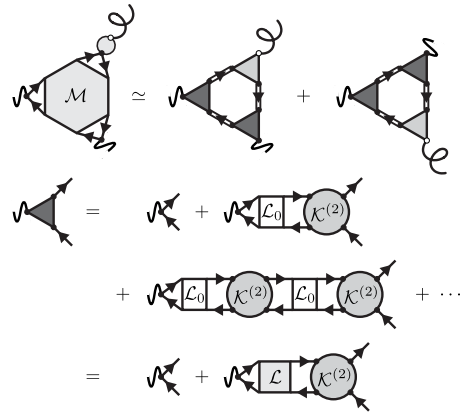


FIG. 1. **Ladder-like approximation to the reduced matrix element for one-phonon Raman scattering.** Top: Diagrammatic approximation for the reduced matrix element (left) as a sum of two terms with effectively opposite orientation of the fermion loop. Dark dots (light circles) denote the bare electron-photon (-phonon) vertex. Double lines denote the one-electron Green's function. Dark (light) shaded triangles the exact electron-photon (-phonon) vertex. Bottom: Exact ladder of diagrams for the electron-light coupling. \mathcal{L} (\mathcal{L}_0) and $\mathcal{K}^{(2)}$ denote the interacting (independent-particle) two-particle correlation function and two-particle interaction kernel, respectively. Note that the same summation is understood to be carried out at each vertex.

used in calculations of optical absorption spectra [25, 26] and is sufficient to capture excitonic effects in hBN [20], MoS₂ [21], and many other materials. In addition, we employ the *Tamm-Dancoff approximation* (TDA), i.e., we neglect the coupling of electronic transitions with positive and negative energy, which is justified for the case of semiconductors with sizable band gap. (ii) The two-particle interaction kernel in the electron-phonon vertex is approximated by a static kernel on the level of time-dependent DFT. This allows us to resum the diagrammatic series for the electron-phonon vertex exactly to obtain an approximation for the electron-phonon coupling that is equivalent to obtaining it via density functional perturbation theory (DFPT) [24]. (iii) We treat the three-particle independent-particle correlation function in the quasi-particle approximation, with the electronic band structure on the level of the *GW* approximation. With these three further approximations, we can give a closed form expression for the reduced Raman matrix element:

$$\begin{aligned}
 \tilde{\mathcal{M}}_{\mu\nu}^\lambda(\omega_L - \omega_D, \omega_D) &= \sum_{S, S'} \frac{d_S^\mu (g_{S, S'}^\lambda)^* (d_{S'}^\nu)^*}{(\omega_L - E_S + i\gamma)(\omega_D - E_{S'} + i\gamma)} \\
 &+ \sum_{S, S'} \frac{(d_S^\mu)^* g_{S, S'}^\lambda d_{S'}^\nu}{(\omega_L + E_S - i\gamma)(\omega_D + E_{S'} - i\gamma)}.
 \end{aligned} \tag{3}$$

Here, the E_S are the exciton energies, γ is a broadening factor that we set to a constant value of 75 meV, and the sums run over all excitonic states of positive energy. The exciton-light and exciton-exciton-phonon matrix elements in the numerators are defined as

$$d_S^\mu \equiv \sum_{\mathbf{k}, \substack{a \in \mathcal{C} \\ b \in \mathcal{V}}} d_{\mathbf{k},a,b}^{\mu,(b)} (A_{\mathbf{k},a,b}^S)^* \quad (4)$$

and

$$g_{S',S}^\lambda \equiv \sum_{\mathbf{k}} \left[\sum_{\substack{a,c \in \mathcal{C} \\ b \in \mathcal{V}}} (A_{\mathbf{k},a,b}^{S'})^* g_{\mathbf{k},a,c}^\lambda A_{\mathbf{k},c,b}^S - \sum_{\substack{a \in \mathcal{C} \\ b,c \in \mathcal{V}}} (A_{\mathbf{k},a,b}^{S'})^* g_{\mathbf{k},c,b}^\lambda A_{\mathbf{k},a,c}^S \right], \quad (5)$$

respectively, where \mathcal{C} (\mathcal{V}) denotes the set of all conduction (valence) band indices. $A_{\mathbf{k},c,v}^S$ denotes an excitonic eigenvector, corresponding to an envelope wave function in transition space, and $d_{\mathbf{k},a,b}^{\mu,(b)}$ and $g_{\mathbf{k},a,b}^\lambda$ denote the bare independent-particle dipole moment and DFPT-level electron-phonon coupling matrix elements, respectively. Details of how to obtain Eq. (3) from Eq. (2) are provided in the SM [23]. Finally, we note that we evaluate the reduced matrix element always in the approximation $\omega_L - \omega_D \approx \omega_\lambda$, which is reasonable for typical phonon decay widths.

As a first test case, we apply our theory to hexagonal boron nitride in its bulk form with AA' stacking order. This material features both strong excitonic effects [20] and light atoms, which leads to relatively large phonon frequencies of up to ≈ 170 meV. The latter makes it an ideal candidate to observe the impact of non-adiabatic effects on the frequency dependence of the resonant Raman intensity. In Fig. 2, we present the results of our calculation for the Raman-active, degenerate, in-plane optical (E_{2g}) phonon mode, summed over outgoing photon and phonon polarizations and averaged over incoming photon polarizations. We show the computed Raman intensity as a function of excitation energy both for the full calculation with excitonic effects (blue lines) and for the independent-particle case (red lines), where we set the two-particle interaction kernel in the electron-photon vertex to zero while still retaining the TDA. In addition, we also compute the Raman intensity both in the full, non-adiabatic theory (full lines) and in the adiabatic limit (dashed lines). As previously shown [19], the latter can be obtained from the former by neglecting the dependence of the reduced matrix element on the phonon frequency. For comparison, we also show the results of a calculation of the imaginary part of the dielectric function, which is closely related to the absorption coefficient.

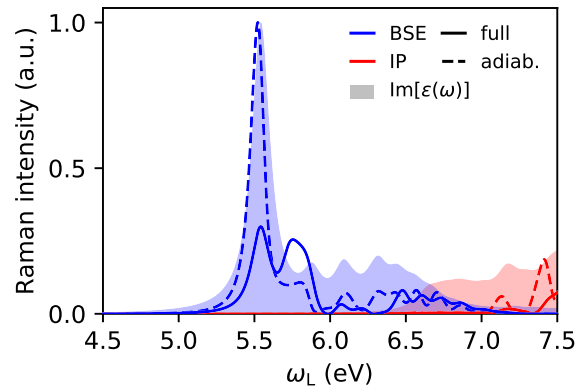


FIG. 2. Calculated Raman intensities for bulk hexagonal boron nitride as a function of excitation frequency. Blue lines: Raman intensity on the BSE-level calculated with the full non-adiabatic theory (full lines) and in the adiabatic limit (dashed lines). Red lines: Same as blue lines, but without excitonic effects, i.e., on the IP-level. Shaded areas: Imaginary part of the dielectric function on the BSE- (blue) and IP-levels (red).

More details of the underlying *ab initio* calculations are given in the SM [23].

In the IP-picture, the absorption spectrum of bulk hBN (red shade) sets on at the direct gap of around 6.50 eV located at the M -point in the band structure (see SM [23]). When excitonic effects are included (blue shade), the absorption spectrum is dominated by a strong excitonic resonance near 5.58 eV, followed by a series of excitonic peaks with less oscillator strength (compare also Refs. [27, 28]).

By contrast, the Raman intensity shows a strikingly different behavior. On the IP-level, the Raman intensity rises only very slowly after the absorption onset. This behavior is typical for hexagonal materials and can be traced back to angular momentum conservation [6, 13, 29]. While the transitions at the direct gap at the M -point are relatively suppressed in the Raman process due to their small dipole moments (see SM [23]), the energetically close transitions around the H -point cannot contribute for symmetry reasons. The latter transitions are located on a circularly symmetric part of the band structure, which implies full angular momentum conservation. This in turn suppresses the Raman scattering process for a degenerate phonon, as the latter carries an effective angular momentum of $\pm\hbar$ and cannot satisfy angular momentum conservation together with the incoming and outgoing photons. The same holds true for the transitions around the K -point, which also possess full rotation symmetry, with the exception of a small valley along the Γ - K direction, which are the only transitions that can contribute to resonant low-energy Raman scattering on the IP-level.

When excitonic effects are included, we observe a strong suppression of the third and fourth excitonic peak. This suppression can be understood by analyzing their composition in \mathbf{k} -space (see SM [23]). The excitonic envelope wave functions of these two excitons are strongly localized around the K -point and are circularly symmetric. As a result, they do not break the full rotation symmetry around the K -point and hence the Raman intensity for a degenerate phonon is again strongly suppressed at these frequencies due to angular momentum conservation. The first two excitons, by contrast, are more delocalized in \mathbf{k} -space and their wave functions already show signs of trigonal warping. Thus the full rotation symmetry is broken down to the 120° -symmetry of the lattice, which then allows the Raman process on symmetry grounds.

Even more interesting though is the comparison to the results obtained within the adiabatic limit (dashed lines in Fig 2). In this limit, the relative weight of the first two excitonic resonances follows that of the absorption spectrum. When non-adiabatic effects are included, however, we observe a strong redistribution of weight from the first to the second exciton. The reason for this is the non-negligible phonon energy of around 170 meV, which is close to the energy difference of the first two excitons (see also SM [23]). From Eq. (3), which is evaluated at $\omega_D = \omega_L - \omega_\lambda$, it is then clear that the two additive contributions from the first two excitons to the reduced matrix element strongly interfere. This illustrates that non-adiabatic effects can play a significant role even in wide-band gap materials and emphasizes the importance of considering both non-adiabatic and excitonic effects at the same time.

We now apply our method to monolayer molybdenum disulfide, which is also known to display strong excitonic effects [28]. MoS_2 features two Raman active modes, a degenerate in-plane mode of symmetry E' and an out-of-plane one of symmetry A'_1 . Furthermore, MoS_2 possesses an electronic band structure that in its optically active region is strongly influenced by spin-orbit coupling [21]. In Fig. 3, we show the results of our calculation for both Raman-active modes, with computational details of the underlying *ab initio* calculations provided in the SM [23]. The optical absorption spectrum of monolayer MoS_2 (blue shade in Fig. 3) is dominated by three strong excitonic resonances, at around 1.971 eV, 2.113 eV, and 3.160 eV. The first two of these are commonly referred to as the “A”- and “B”-exciton [30], while the latter resonance actually consists of several excitons around a main one, which we will refer to as the “C”-exciton. The \mathbf{k} -point-resolved envelope wave functions of the “A”- and “B”-excitons are strongly localized around the K -point (see SM [23]) and the difference in energy corresponds to the spin-orbit coupling-induced splitting of the valence

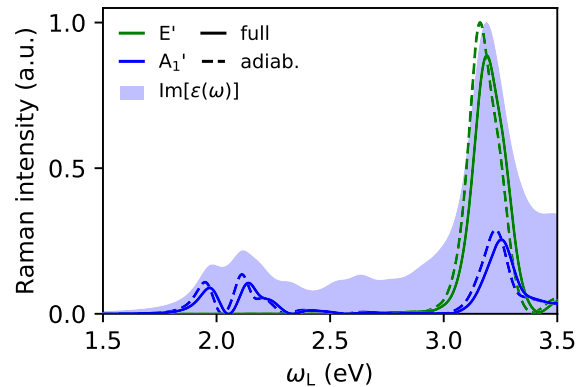


FIG. 3. **Calculated Raman intensities for monolayer molybdenum disulfide as a function of excitation frequency.** Green and blue lines: Raman intensity of the E' - (green) and A'_1 -modes (blue) on the BSE-level calculated with the full non-adiabatic theory (full lines) and in the adiabatic limit (dashed lines). Blue shaded area: Imaginary part of the dielectric function on the BSE-level.

band. By contrast, the dominant “C”-exciton is strongly delocalized in \mathbf{k} -space.

The Raman spectrum of the A'_1 -mode (blue line) closely follows this trend. Due to the double resonant structure of the reduced matrix element, the excitonic peaks become more pronounced and well-separated, for example, in the case of the “A”- and “B”-excitons. The degenerate E' -mode, on the other hand, does not show any resonances at the energies of the “A”- and “B”-excitons. This can again be traced back to their envelope wave functions being strongly localized around the K -point, where the band structure exhibits full rotation symmetry (see SM [23]), which in turn suppresses Raman scattering due to angular momentum conservation. In the region around the “C”-exciton, however, the excitons couple much more strongly to the E' -mode than to the A'_1 -mode. This behavior can be understood from an analysis of the exciton-phonon coupling (see SM [23]). In the energy-regime of the “C”-exciton, the E' -mode couples different bright excitons with one another, which then all contribute to the Raman intensity. The A'_1 -mode, however, does not couple different excitons but, due to its scalar nature, can only lead to intra-exciton scattering. As a result, there are much fewer contributions to the corresponding matrix element, which results in the E' -mode featuring a much larger intensity than the A'_1 -mode in the exciton continuum. This analysis also corrects the controversial statement of the recent Ref. [18] that only inter-exciton scattering should be considered in the resonant regime, i.e., the “A”- and “B”-excitons should be silent, which is in stark contrast to experiments of other monolayer transition metal dichalcogenites [6].

Finally, we comment on the effects of non-adiabaticity

in the case of MoS₂. Here, the phonon energies of the Raman active modes are on the order of 50 meV [30]. This is not enough to overcome the spin-orbit coupling-induced splitting of the “A”- and “B”-excitons of around 110 meV. The contributions from the “A”- and “B”-excitonic resonances to the reduced matrix element are thus prevented from interfering with one another. Instead, the inclusion of non-adiabatic effects only results in a blueshift of all resonances compared to the adiabatic case (dashed lines in Fig. 3).

In conclusion, we have presented a method for the computation of resonant one-phonon Raman intensities from first principles that takes into account both excitonic and non-adiabatic effects. We have applied our method to both bulk hexagonal boron nitride and single-layer molybdenum disulfide. In the case of the former, we have explained the absence of particular higher excitonic resonances from the Raman intensity spectrum with angular momentum conservation. More importantly, we have proven the significance of non-adiabaticity for the Raman process, as it leads to strong quantum interference between the first two excitonic resonances. For MoS₂, we have shown that spin-orbit splitting protects the lowest two excitonic resonances from non-adiabatic effects. Furthermore, we have explained the different behavior of the two Raman active modes from their intra- and inter-exciton-phonon couplings.

The authors acknowledge the use of the QuantumESPRESSO suite [31] for the DFT calculations within the local density approximation [32], the yambo code [33] and the SLEPc [34] library for the MBPT calculations, and usage of the HPC facilities of the University of Luxembourg [35]. The authors would further like to thank A. Marini for inspiring discussions. S.R. and L.W. acknowledge financial support by the National Research Fund (FNR) Luxembourg (projects RAM-GRASEA and INTER/ANR/13/20/NANOTMD). S.R. also acknowledges financial support by the Leverhulme Trust (Grant RL-2012-001).

[1] P.-H. Tan, ed., *Raman Spectroscopy of Two-Dimensional Materials* (Springer, Berlin, 2018).
 [2] J. Sonntag, S. Reichardt, L. Wirtz, B. Beschoten, M. I. Katsnelson, F. Libisch, and C. Stampfer, *Phys. Rev. Lett.* **120**, 187701 (2018).
 [3] S. Pisana, M. Lazzeri, C. Casiraghi, K. S. Novoselov, A. K. Geim, A. C. Ferrari, and F. Mauri, *Nat. Mater.* **6**, 198 (2007).
 [4] J. Yan, Y. Zhang, P. Kim, and A. Pinczuk, *Phys. Rev. Lett.* **98**, 166802 (2007).

[5] B. R. Carvalho, L. M. Malard, J. M. Alves, C. Fantini, and M. A. Pimenta, *Phys. Rev. Lett.* **114**, 136403 (2015).
 [6] H. P. C. Miranda, S. Reichardt, G. Froehlicher, A. Molina-Sánchez, S. Berciaud, and L. Wirtz, *Nano Lett.* **17**, 2381 (2017).
 [7] V. N. Popov and P. Lambin, *Phys. Rev. B* **73**, 165425 (2006).
 [8] D. M. Basko, *Phys. Rev. B* **78**, 125418 (2008).
 [9] D. M. Basko, *New. J. Phys.* **11**, 095011 (2009).
 [10] P. Venezuela, M. Lazzeri, and F. Mauri, *Phys. Rev. B* **84**, 035433 (2011).
 [11] F. Herzig, M. Calandra, P. Gava, P. May, M. Lazzeri, F. Mauri, and J. Maultzsch, *Phys. Rev. Lett.* **113**, 187401 (2014).
 [12] E. H. Hasdeo, A. R. T. Nugraha, M. S. Dresselhaus, and R. Saito, *Phys. Rev. B* **94**, 075104 (2016).
 [13] S. Reichardt and L. Wirtz, *Phys. Rev. B* **95**, 195422 (2017).
 [14] P. Knoll and C. Ambrosch-Draxl, in *Proceedings of the international workshop on anharmonic properties of high-*T_c* cuprates*, edited by D. Mihailovic, G. Ruani, E. Kalids, and K. A. Müller (World Scientific, 1995) p. 220.
 [15] C. Ambrosch-Draxl, H. Auer, R. Kouba, E. Y. Sherman, P. Knoll, and M. Mayer, *Phys. Rev. B* **65**, 064501 (2002).
 [16] Y. Gillet, M. Giantomassi, and X. Gonze, *Phys. Rev. B* **88**, 094305 (2013).
 [17] Y. Gillet, S. Kontur, M. Giantomassi, C. Draxl, and X. Gonze, *Sci. Rep.* **7**, 7344 (2017).
 [18] Y. Wang, B. R. Carvalho, and V. H. Crespi, *Phys. Rev. B* **98**, 161405(R) (2018).
 [19] S. Reichardt and L. Wirtz, Submitted, arXiv:1808.08212 (2018).
 [20] B. Arnaud, S. Lebègue, P. Rabiller, and M. Alouani, *Phys. Rev. Lett.* **96**, 026402 (2006).
 [21] A. Molina-Sánchez, M. Palummo, A. Marini, and L. Wirtz, *Phys. Rev. B* **93**, 155435 (2016).
 [22] S. Reich, A. C. Ferrari, R. Arenal, A. Loiseau, I. Bello, and J. Robertson, *Phys. Rev. B* **71**, 205201 (2005).
 [23] See Supplemental Material for additional theoretical and computational details.
 [24] S. Reichardt, *Many-Body Perturbation Theory Approach to Raman Spectroscopy and Its Application to 2D Materials*, Ph.D. thesis, RWTH Aachen University & University of Luxembourg (2018).
 [25] F. Bechstedt, *Many-Body Approach to Electronic Excitations* (Springer, Berlin, 2016).
 [26] R. M. Martin, L. Reining, and D. M. Ceperley, *Interacting Electrons* (Cambridge University Press, Cambridge, 2016).
 [27] T. Galvani, F. Paleari, H. P. C. Miranda, A. Molina-Sánchez, L. Wirtz, S. Latil, H. Amara, and F. Ducastelle, *Phys. Rev. B* **94**, 125303 (2016).
 [28] W. Aggoune, C. Cocchi, D. Nabok, K. Rezouali, M. A. Belkhir, and C. Draxl, *Phys. Rev. B* **97**, 241114(R) (2018).
 [29] S. Reichardt and L. Wirtz, in *Optical Properties of Graphene*, edited by R. Binder (World Scientific, Singapore, 2017) Chap. 3, pp. 85–132.
 [30] A. Molina-Sánchez, D. Sangalli, K. Hummer, A. Marini, and L. Wirtz, *Phys. Rev. B* **88**, 045412 (2013).
 [31] P. Giannozzi, S. Baroni, N. Bonini, M. Calandra, R. Car, C. Cavazzoni, D. Ceresoli, G. L. Chiarotti, M. Cococcioni, I. Dabo, A. Dal Corso, S. de Gironcoli, S. Fabris, G. Fratesi, R. Gebauer, U. Gerstmann, C. Gougoussis,

- A. Kokalj, M. Lazzeri, L. Martin-Samos, N. Marzari, F. Mauri, R. Mazzarello, S. Paolini, A. Pasquarello, L. Paulatto, C. Sbraccia, S. Scandolo, G. Sclauzero, A. P. Seitsonen, A. Smogunov, P. Umari, and R. M. Wentzcovitch, *J. Phys. Condens. Matter* **21**, 395502 (2009).
- [32] J. P. Perdew and A. Zunger, *Phys. Rev. B* **23**, 5048 (1981).
- [33] A. Marini, C. Hogan, M. Grüning, and D. Varsano, *Comput. Phys. Commun.* **180**, 1392 (2009).
- [34] V. Hernandez, J. E. Roman, and V. Vidal, *ACM Trans. Math. Softw.* **31**, 351 (2005).
- [35] S. Varrette, P. Bouvry, H. Cartiaux, and F. Georgatos, in *2014 International Conference on High Performance Computing & Simulation (HPCS)* (IEEE, 2014) pp. 959–967.

Non-adiabatic effects in exciton-mediated Raman scattering from first principles – Supplemental Material

Sven Reichardt^{1,2} and Ludger Wirtz²

¹*Department of Materials, University of Oxford,
Parks Road, Oxford OX1 3PH, United Kingdom*

²*Physics and Materials Science Research Unit,
University of Luxembourg, 1511 Luxembourg, Luxembourg*

The Supplemental Material is structured as follows:

In Section S1, we provide additional theoretical details for our approach. Section S2 contains supplementary information on the calculation for bulk hexagonal boron nitride (hBN). Finally, we present supplementary material for the calculation for monolayer molybdenum disulfide (MoS₂) in Section S3.

S1. THEORETICAL DETAILS

Here we provide more details on how to obtain Eq. (3) from Eq. (2) of the main text within the specified approximations.

First, we expand the (bare) electronic current density and force operators in a basis of Kohn-Sham states:

$$\hat{J}_\mu \equiv \sum_{\mathbf{k}, a, a'} \left(d_{\mathbf{k}, a', a}^{\mu, (b)} \right)^* \hat{c}_{\mathbf{k}, a}^\dagger \hat{c}_{\mathbf{k}, a'} \quad (\text{S1})$$

$$\hat{F}_\lambda \equiv \sum_{\mathbf{k}, b, b'} \left(g_{\mathbf{k}, b', b}^{\lambda, (b)} \right)^* \hat{c}_{\mathbf{k}, b}^\dagger \hat{c}_{\mathbf{k}, b'}. \quad (\text{S2})$$

The expansion coefficients are defined such that they denote the matrix elements for *photon/phonon emission*, i.e., *current density/force annihilation*. Note that at zero momentum transfer and for real polarization vectors/phonon eigenvectors, the matrix elements obey $m_{\mathbf{k}, a', a}^{(b)} = \left(m_{\mathbf{k}, a, a'}^{(b)} \right)^*$.

In terms of these matrix elements, the force-current-current correlation function reads

$$\begin{aligned} \langle 0 | \mathcal{T} \left[\hat{F}_\lambda(t') \hat{J}_\nu(t) \hat{J}_\mu^\dagger(0) \right] | 0 \rangle \Big|_{\text{connect.}} &= \sum_{\mathbf{k}, \mathbf{k}', \mathbf{k}''} \sum_{\substack{a, b, c \\ a', b', c'}} \left(g_{\mathbf{k}, a', a}^{\lambda, (b)} \right)^* \left(d_{\mathbf{k}', b', b}^{\nu, (b)} \right)^* d_{\mathbf{k}'', c, c'}^{\mu, (b)} \\ &\times \langle 0 | \mathcal{T} \left[\hat{c}_{\mathbf{k}, a}^\dagger(t') \hat{c}_{\mathbf{k}, a'}(t') \hat{c}_{\mathbf{k}', b}^\dagger(t) \hat{c}_{\mathbf{k}', b'}(t) \hat{c}_{\mathbf{k}'', c}^\dagger(0) \hat{c}_{\mathbf{k}'', c'}(0) \right] | 0 \rangle \Big|_{\text{connect.}}. \end{aligned} \quad (\text{S3})$$

The last factor is the fully connected part of the three-particle Green's function. We approximate it in a controlled way with the help of Feynman diagrams, as shown in Fig. S1. The first term shown corresponds to

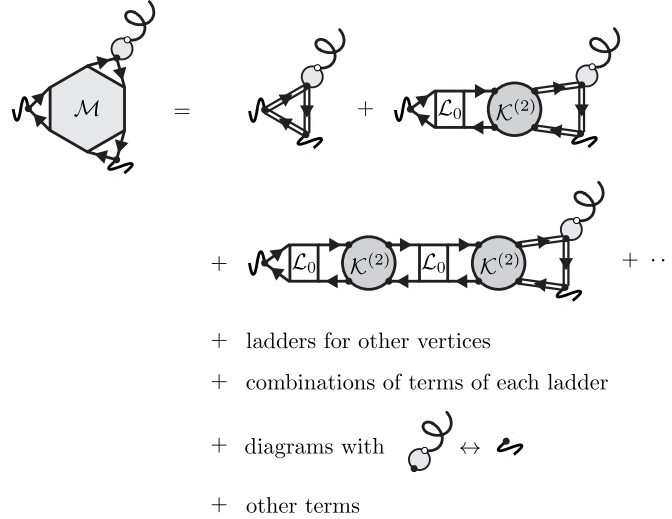


FIG. S1. **Diagrammatic analysis of the reduced matrix element.** Dark dots (light circles) denote the bare electron-photon (-phonon) vertex. Double lines denote the one-electron Green's function. \mathcal{L} (\mathcal{L}_0) and $\mathcal{K}^{(2)}$ denote the interacting (independent-particle) two-particle correlation function and two-particle interaction kernel, respectively.

the independent-particle approximation to the three-particle correlation function. In the second term, we include the first-order correction to the electron-incoming photon vertex due to two-particle inter-electron interactions. We denote the kernel describing the letter by $\mathcal{K}^{(2)}$, while \mathcal{L}_0 represents the two-particle correlation function on the independent-particle level. The second line shows the second-order correction to the same vertex while the dots refer to higher-order correction of the same form. We consider the same summation of terms for all three vertices simultaneously. In order to consider all topologically distinct diagrams, we also need to consider terms in which the fermion flow is reversed, i.e., in which the vertices for the outgoing photon and phonon are interchanged.

The *ladder-like approximation* introduced in the main text now consists of neglecting all other terms that do not follow the ladder-like structure depicted in the first two lines of Fig. S1. As shown in Fig. 1 of the main text, the summation of terms at each vertex can be carried out separately. The double Fourier transform of the force-current-current correlation function, which up to a factor of i corresponds to the reduced matrix element,

then takes on the form

$$i\tilde{\mathcal{M}}_{\mu\nu}^{\lambda}(\omega', \omega) = \sum_{\mathbf{k}} \sum_{\substack{a,b,c \\ a',b',c'}} \bar{g}_{\mathbf{k},a',a}^{\lambda}(\omega') \bar{d}_{\mathbf{k},b',b}^{\nu}(\omega) d_{\mathbf{k},c,c'}^{\mu}(\omega + \omega') \\ \times \int_{-\infty}^{+\infty} dt e^{i\omega t} \int_{-\infty}^{+\infty} dt' e^{i\omega' t'} \langle 0 | \mathcal{T} \left[\hat{c}_{\mathbf{k},a}^{\dagger}(t) \hat{c}_{\mathbf{k},a'}(t') \hat{c}_{\mathbf{k},b}^{\dagger}(t) \hat{c}_{\mathbf{k},b'}(t) \hat{c}_{\mathbf{k},c}^{\dagger}(0) \hat{c}_{\mathbf{k},c'}(0) \right] | 0 \rangle \Big|_{\text{IP,connect.}}, \quad (\text{S4})$$

where the three-particle correlation function now only appears in the form of its independent-particle version. The first three factors denote the Fourier transforms of the *exact* vertices, with a bar denoting the vertices for photon/phonon emission. To obtain concrete expressions for the latter, we approximate the two-particle interaction kernel as mentioned in the main text.

In the case of the electron-light vertex, we approximate it as the sum of a statically screened, attractive electron-hole Coulomb interaction and a bare, repulsive exchange part. We can then give an explicit expression for the Fourier-transformed vertex function by making use of the Bethe-Salpeter equation

$$L_{\mathbf{k},a',a}^{\mu}(\omega) = L_{0;\mathbf{k},a',a}(\omega) \delta_{\mathbf{k},\mathbf{k}'} \delta_{a',b'} \delta_{a,b} + L_{0;\mathbf{k},a',a}(\omega) \sum_{\mathbf{k}''} \sum_{c',c} K_{\mathbf{k},a',a}^{(2)} L_{\mathbf{k}'',c',c}^{\mu}(\omega) \quad (\text{S5})$$

where we now use non-calligraphic script to denote the approximated quantities. Note that we also use the quasi-particle approximation for L_0 , so that it only depends on two band indices. As shown in Fig. 1 of the main text, we can identify the right-hand side up to a factor of L_0 as the factor that modulates the bare vertex, and we thus have

$$d_{\mathbf{k},a',a}^{\mu}(\omega) = d_{\mathbf{k},a',a}^{\mu,(b)} + \sum_{\mathbf{k}',\mathbf{k}''} \sum_{\substack{b',c' \\ b,c}} K_{\mathbf{k},a',a}^{(2)} L_{\mathbf{k}',b',b}(\omega) d_{\mathbf{k}'',c',c}^{\mu,(b)} = L_{0;\mathbf{k},a',a}^{-1}(\omega) \sum_{\mathbf{k}'} \sum_{b',b} L_{\mathbf{k},a',a}(\omega) d_{\mathbf{k}',b',b}^{\mu,(b)} \quad (\text{S6})$$

for photon *absorption* and

$$\bar{d}_{\mathbf{k},a',a}^{\mu}(\omega) = \left(d_{\mathbf{k},a',a}^{\mu,(b)} \right)^* + \sum_{\mathbf{k}',\mathbf{k}''} \sum_{\substack{b',c' \\ b,c}} \left(d_{\mathbf{k}',b',b}^{\mu,(b)} \right)^* L_{\mathbf{k}'',c',c}(\omega) K_{\mathbf{k},a',a}^{(2)} = \sum_{\mathbf{k}'} \sum_{b',b} \left(d_{\mathbf{k}',b',b}^{\mu,(b)} \right)^* L_{\mathbf{k},a',a}(\omega) L_{0;\mathbf{k},a',a}^{-1}(\omega). \quad (\text{S7})$$

for photon *emission*. Lastly, as mentioned in the main text, we also use the *Tamm-Dancoff approximation*, which is justified for the semiconducting systems discussed in the main text. In this approximation, the independent-particle two-particle correlation function reads

$$L_{0;\mathbf{k},a',a}(\omega) = \frac{\bar{f}_{\mathbf{k},a'} f_{\mathbf{k},a}}{\omega - (\varepsilon_{\mathbf{k},a'} - \varepsilon_{\mathbf{k},a}) + i\eta} + \frac{f_{\mathbf{k},a'} \bar{f}_{\mathbf{k},a}}{-\omega - (\varepsilon_{\mathbf{k},a} - \varepsilon_{\mathbf{k},a'}) + i\eta}, \quad (\text{S8})$$

where $f_{\mathbf{k},a}$ denotes the occupancy of the state $|\mathbf{k}, a\rangle$ in the ground state and $\bar{f}_{\mathbf{k},a} \equiv 1 - f_{\mathbf{k},a}$. The interacting two-particle correlation function can be expressed in terms of the excitonic wave functions $A_{\mathbf{k},a',a}^S$ and energies E_S as

$$L_{\mathbf{k},a',a}^{\mu}(\omega) = \sum_S \left[\bar{f}_{\mathbf{k},a'} f_{\mathbf{k},a} \bar{f}_{\mathbf{k}',b'} f_{\mathbf{k}',b} \frac{A_{\mathbf{k},a',a}^S (A_{\mathbf{k}',b',b}^S)^*}{\omega - E_S + i\eta} + f_{\mathbf{k},a'} \bar{f}_{\mathbf{k},a} f_{\mathbf{k}',b'} \bar{f}_{\mathbf{k}',b} \frac{(A_{\mathbf{k},a,a'}^S)^* A_{\mathbf{k}',b',b}^S}{-\omega - E_S + i\eta} \right], \quad (\text{S9})$$

where the sum runs over all *positive-energy* excitons. Note that within the Tamm-Dancoff approximation, an excitonic envelope wave function $A_{\mathbf{k},a',a}^S$ for positive-energy excitons has non-vanishing components only for $a' \in \mathcal{C}$ and $a \in \mathcal{V}$, where \mathcal{C} and \mathcal{V} denote the sets of conduction and valence band indices, respectively. Combining the last three equations, we arrive at the final expression we use to approximate the exact electron-photon vertices:

$$d_{\mathbf{k},a',a}^{\mu}(\omega) = \sum_S \left[\bar{f}_{\mathbf{k},a'} f_{\mathbf{k},a} A_{\mathbf{k},a',a}^S \frac{\omega - (\varepsilon_{\mathbf{k},a'} - \varepsilon_{\mathbf{k},a}) + i\eta}{\omega - E_S + i\eta} d_S^{\mu} \right. \\ \left. + f_{\mathbf{k},a'} \bar{f}_{\mathbf{k},a} (A_{\mathbf{k},a,a'}^S)^* \frac{-\omega - (\varepsilon_{\mathbf{k},a} - \varepsilon_{\mathbf{k},a'}) + i\eta}{-\omega - E_S + i\eta} (d_S^{\mu})^* \right] \quad (\text{S10})$$

and

$$\bar{d}_{\mathbf{k},a',a}^{\mu}(\omega) = \sum_S \left[\bar{f}_{\mathbf{k},a'} f_{\mathbf{k},a} (d_S^{\mu})^* \frac{\omega - (\varepsilon_{\mathbf{k},a'} - \varepsilon_{\mathbf{k},a}) + i\eta}{\omega - E_S + i\eta} (A_{\mathbf{k},a',a}^S)^* \right. \\ \left. + f_{\mathbf{k},a'} \bar{f}_{\mathbf{k},a} d_S^{\mu} \frac{-\omega - (\varepsilon_{\mathbf{k},a} - \varepsilon_{\mathbf{k},a'}) + i\eta}{-\omega - E_S + i\eta} A_{\mathbf{k},a,a'}^S \right], \quad (\text{S11})$$

with d_S^μ as defined in Eq. (4) of the main text.

For the exact electron-phonon vertex, we follow the same line of argument, but approximate the two-particle interaction kernel in that case with the kernel corresponding to time-dependent density functional theory. As shown in Ref. [1], this approximation is exactly equivalent to using the statically screened electron-phonon coupling on the level of density functional perturbation theory. In addition, we also neglect the frequency dependence of the vertex function, i.e., we use

$$\bar{g}_{\mathbf{k},a',a}^\lambda(\omega) \rightarrow (g_{\mathbf{k},a',a}^\lambda)^* \Big|_{\text{DFPT}}, \quad (\text{S12})$$

which is justified for systems with a band gap much larger than the phonon frequency. Note, however, that we *do retain the phonon frequency-dependence of the three-particle independent-particle correlation function* as there the frequency of the photon needs to be considered as well, which reduces the effective band gap seen by the phonon in the three-particle correlation function.

Finally, we also give the explicit form of the Fourier transformed independent-particle three-particle correlation function. Treating it on the level of the quasi-particle approximation, we find

$$\begin{aligned} & \int_{-\infty}^{+\infty} dt e^{i\omega t} \int_{-\infty}^{+\infty} dt' e^{i\omega' t'} \langle 0 | \mathcal{T} \left[\hat{c}_{\mathbf{k},a}^\dagger(t') \hat{c}_{\mathbf{k},a'}(t') \hat{c}_{\mathbf{k},b}^\dagger(t) \hat{c}_{\mathbf{k},b'}(t) \hat{c}_{\mathbf{k},c}^\dagger(0) \hat{c}_{\mathbf{k},c'}(0) \right] | 0 \rangle \Big|_{\text{IP,connect.}} \\ &= \int_{-\infty}^{+\infty} dt e^{i\omega t} \int_{-\infty}^{+\infty} dt' e^{i\omega' t'} (-1) \\ & \quad \times \left\{ \delta_{a',b} \delta_{b',c} \delta_{c',a} \langle 0 | \mathcal{T} \left[\hat{c}_{\mathbf{k},a}(t') \hat{c}_{\mathbf{k},a}^\dagger(t) \right] | 0 \rangle \langle 0 | \mathcal{T} \left[\hat{c}_{\mathbf{k},b}(t) \hat{c}_{\mathbf{k},b}^\dagger(0) \right] | 0 \rangle \langle 0 | \mathcal{T} \left[\hat{c}_{\mathbf{k},c}(0) \hat{c}_{\mathbf{k},c}^\dagger(t') \right] | 0 \rangle \right. \\ & \quad \left. + \delta_{a',c} \delta_{c',b} \delta_{b',a} \langle 0 | \mathcal{T} \left[\hat{c}_{\mathbf{k},a}(t') \hat{c}_{\mathbf{k},a}^\dagger(0) \right] | 0 \rangle \langle 0 | \mathcal{T} \left[\hat{c}_{\mathbf{k},b}(t) \hat{c}_{\mathbf{k},b}^\dagger(t') \right] | 0 \rangle \langle 0 | \mathcal{T} \left[\hat{c}_{\mathbf{k},c}(0) \hat{c}_{\mathbf{k},c}^\dagger(t) \right] | 0 \rangle \right\} \\ & \equiv i \delta_{a',b} \delta_{b',c} \delta_{c',a} R_{0;\mathbf{k},c,a,b}(-\omega', -\omega) + i \delta_{a',c} \delta_{c',b} \delta_{b',a} R_{0;\mathbf{k},a,b,c}(\omega', \omega). \end{aligned} \quad (\text{S13})$$

In the last step, we identified the Fourier transform of the independent-particle three-particle correlation function on the quasi-particle level, which is explicitly given by

$$\begin{aligned} & (-i) R_{0;\mathbf{k},a,b,c}(\omega_1, \omega_2) \\ & \equiv \int_{-\infty}^{+\infty} dt e^{i\omega t} \int_{-\infty}^{+\infty} dt' e^{i\omega' t'} \langle 0 | \mathcal{T} \left[\hat{c}_{\mathbf{k},a}(t') \hat{c}_{\mathbf{k},a}^\dagger(0) \right] | 0 \rangle \langle 0 | \mathcal{T} \left[\hat{c}_{\mathbf{k},b}(t) \hat{c}_{\mathbf{k},b}^\dagger(t') \right] | 0 \rangle \langle 0 | \mathcal{T} \left[\hat{c}_{\mathbf{k},c}(0) \hat{c}_{\mathbf{k},c}^\dagger(t) \right] | 0 \rangle \\ & = + \frac{f_{\mathbf{k},a} \bar{f}_{\mathbf{k},b} \bar{f}_{\mathbf{k},c}}{[-\omega_1 - \omega_2 - (\varepsilon_{\mathbf{k},c} - \varepsilon_{\mathbf{k},a}) + i\eta][-\omega_1 - (\varepsilon_{\mathbf{k},b} - \varepsilon_{\mathbf{k},a}) + i\eta]} \\ & \quad - \frac{\bar{f}_{\mathbf{k},a} f_{\mathbf{k},b} f_{\mathbf{k},c}}{[\omega_1 + \omega_2 - (\varepsilon_{\mathbf{k},a} - \varepsilon_{\mathbf{k},c}) + i\eta][\omega_1 - (\varepsilon_{\mathbf{k},a} - \varepsilon_{\mathbf{k},b}) + i\eta]} \\ & \quad + \frac{\bar{f}_{\mathbf{k},a} \bar{f}_{\mathbf{k},b} f_{\mathbf{k},c}}{[\omega_1 + \omega_2 - (\varepsilon_{\mathbf{k},a} - \varepsilon_{\mathbf{k},c}) + i\eta][\omega_2 - (\varepsilon_{\mathbf{k},b} - \varepsilon_{\mathbf{k},c}) + i\eta]} \\ & \quad - \frac{f_{\mathbf{k},a} f_{\mathbf{k},b} \bar{f}_{\mathbf{k},c}}{[-\omega_1 - \omega_2 - (\varepsilon_{\mathbf{k},c} - \varepsilon_{\mathbf{k},a}) + i\eta][-\omega_2 - (\varepsilon_{\mathbf{k},c} - \varepsilon_{\mathbf{k},b}) + i\eta]} \\ & \quad + \frac{\bar{f}_{\mathbf{k},a} f_{\mathbf{k},b} \bar{f}_{\mathbf{k},c}}{[\omega_1 - (\varepsilon_{\mathbf{k},a} - \varepsilon_{\mathbf{k},b}) + i\eta][-\omega_2 - (\varepsilon_{\mathbf{k},c} - \varepsilon_{\mathbf{k},b}) + i\eta]} \\ & \quad - \frac{f_{\mathbf{k},a} \bar{f}_{\mathbf{k},b} f_{\mathbf{k},c}}{[-\omega_1 - (\varepsilon_{\mathbf{k},b} - \varepsilon_{\mathbf{k},a}) + i\eta][\omega_2 - (\varepsilon_{\mathbf{k},b} - \varepsilon_{\mathbf{k},c}) + i\eta]}. \end{aligned} \quad (\text{S14})$$

It is then straightforward to obtain Eqs. (3-5) from the main text by combining all of the individual pieces.

S2. SUPPLEMENTARY INFORMATION FOR THE HBN CALCULATION

In this section, we provide more computational details for the calculations for bulk hexagonal boron nitride. We also show the electronic band structure and the exciton spectrum. For the latter, we show the oscillator strength and the exciton-phonon coupling. Finally, we provide a plot of the excitonic envelope wave functions in reciprocal space for the first four optically active excitons.

Computational details

The ground state properties of bulk hexagonal boron nitride in the AA' stacking configuration were computed on the level of density functional theory (DFT) within the local density approximation (LDA) for the exchange-correlation functional in the parametrization due to Perdew and Zunger [2]. All DFT calculations were performed with the `Pwscf` code of the `QuantumESPRESSO` suite [3] using norm-conserving, non-relativistic, core-corrected pseudopotentials. We use a plane-wave basis set with an energy cutoff of 110 Ry for the electronic wave functions and 440 Ry for the charge density. For integrations over the first Brillouin zone, a uniform \mathbf{k} -point mesh of size $12 \times 12 \times 2$ was used. The lattice parameters were relaxed prior to the calculation, yielding values of $a=2.478 \text{ \AA}$ and $c=6.453 \text{ \AA}$ for the in- and out-of-plane lattice constants, respectively. For the electronic excited state properties, we computed the electronic band structure on a $36 \times 36 \times 2$ \mathbf{k} -point mesh for 200 (spin-degenerate) bands.

The calculation of the excitonic eigenenergies and envelope wave functions was performed with the `yambo` code [4]. The two-particle interaction kernel was computed on the level of the Tamm-Dancoff approximation as the sum of a statically screened attractive Coulomb part plus a repulsive bare exchange part. The static inverse dielectric screening function was computed on the level of the random phase approximation using plane-wave cutoffs of 60 Ry each for the electronic wave functions and the dielectric response function in reciprocal space. For the calculation of the actual two-particle interaction kernel, we truncated the attractive screened Coulomb part at a plane-wave energy cutoff of 10 Ry and the repulsive bare exchange part at a plane-wave cutoff of 20 Ry. We included the upper two valence and lower two conduction bands in the construction of the two-particle interaction kernel. A rigid band shift of 2 eV was added to all independent-particle transition energies in order to account for the underestimation of the band gap in DFT. This value was obtained in previous first principle calculations on the level of the GW approximation [5]. Finally, we solve the Bethe-Salpeter equation iteratively for the first 2000 excitonic eigenenergies and envelope wave functions using the `SLEPc` library [6].

For the screened electron-phonon coupling, we approximate the two-particle interaction kernel on the level of time-dependent density functional theory. As this approximation is equivalent to obtaining the screened electron-phonon matrix elements with density functional perturbation theory [1], we calculate the screened matrix elements with the `PH` code of the `QuantumESPRESSO` suite [3]. Lastly, for the phonon frequency of the degenerate, Raman-active in-plane optical mode (E_{2g} -symmetry), we use the calculated value of 1388.6 cm^{-1} .

Electronic band structure

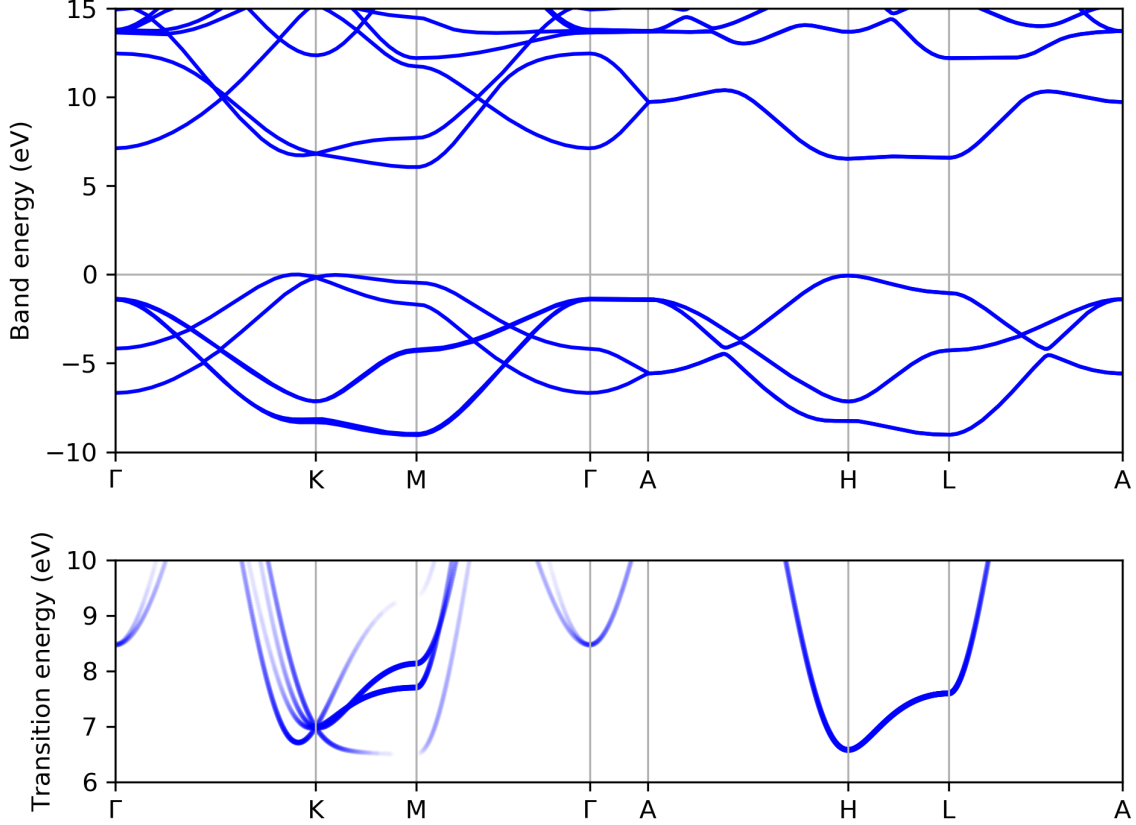


FIG. S2. **hBN: Electronic (transition) band structure.** Top: Electronic band structure on the level of Kohn-Sham DFT within the LDA. A rigid shift of 2 eV was added to all conduction band energies. Bottom: Electronic transition band structure obtained from the electronic band structure. The opacity of the lines corresponds to the optical activity of the transition.

The electronic band structure of bulk hexagonal boron nitride is shown in Fig. S2. We show both the electronic band structure on the level of Kohn-Sham DFT on the LDA-level (top panel) and the resulting transition band structure weighted by the absolute value of the in-plane polarization-averaged transition dipole matrix element squared (bottom panel). As mentioned in the previous section, we shifted all conduction bands by 2 eV to account for the underestimation of the band gap in DFT [5].

The band structure is characterized by an indirect gap of 6.038 eV between the top of the valence band near the K -point and the bottom of the conduction band at the M -point. The direct gap of 6.500 eV is located at M and is quasi-degenerate with the transition at H . The low-energy electronic transitions are located around the M -, H -, and K -points as well as on the line K - M .

Near the band gap, i.e., in the vicinity of the M - and H -points, the electronic transitions are either only weakly optically inactive (M -point) or the band structure is circularly symmetric (H -point). In case of the former the respective transitions are trivially prevented from participating in the Raman scattering process. In case of the latter, the full rotation symmetry leads to full angular momentum conservation, which in turn suppresses scattering involving the degenerate E_{2g} -phonon, as argued in the main text. This explains the absence of a sizable Raman intensity near the band edge on the independent-particle level.

For the exciton physics the most important region is the the immediate neighborhood of the K -point, as the overtone excitons are mostly composed of transitions from there. Close to K , the low-energy transition band structure is circularly symmetric, i.e., for the physics that involves only these transitions, the system again behaves as if it possessed full rotation symmetry. This argument is used in the main text when the principle of angular momentum conservation is invoked to discuss the suppression of the Raman intensity for the overtone excitons. A bit further away from K , the valley along the Γ - K direction breaks the full rotation symmetry, which allows the excitons that more delocalized in \mathbf{k} -space to contribute to the Raman scattering process.

Exciton spectrum: Oscillator strength and exciton-phonon coupling

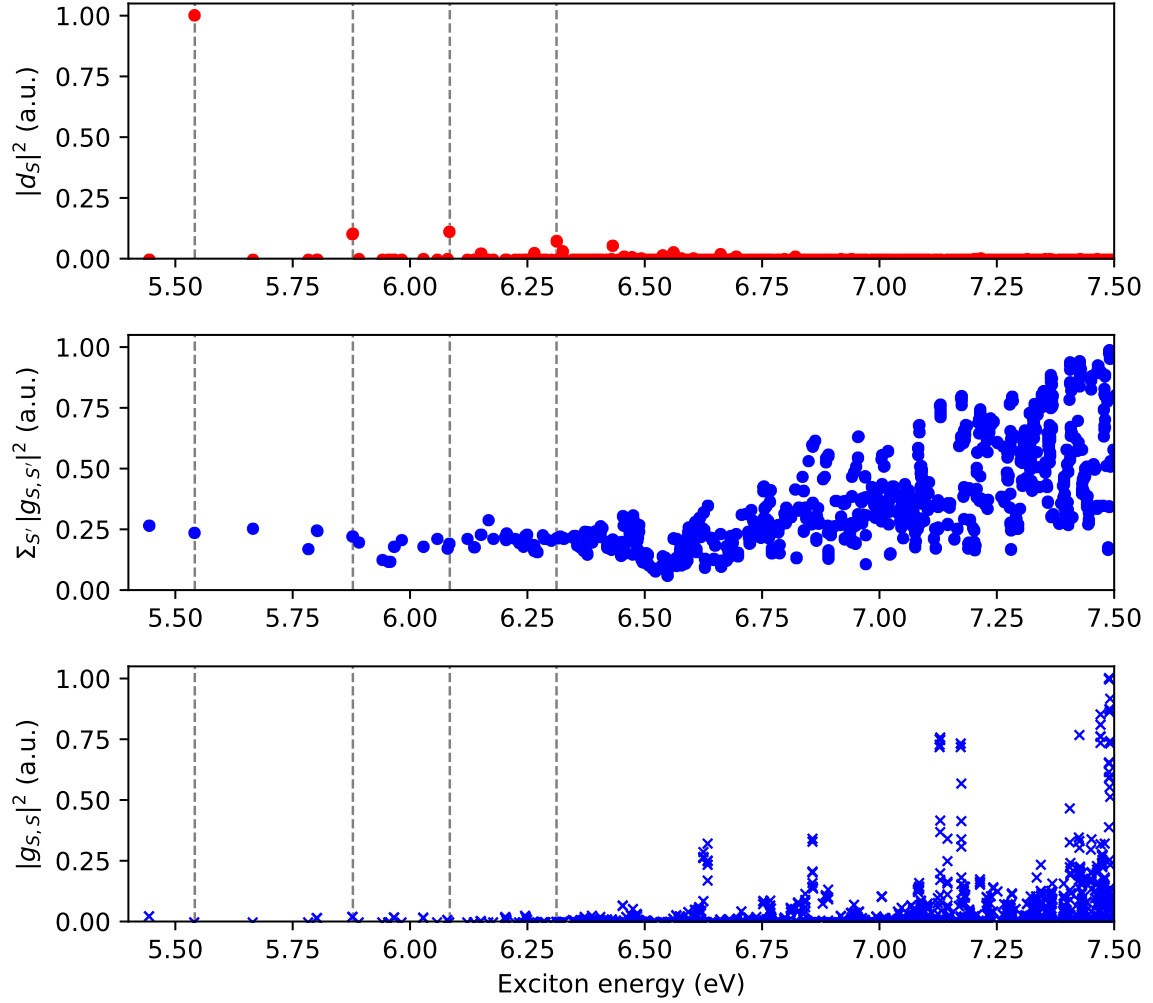


FIG. S3. **hBN: Oscillator strength and exciton-phonon coupling as a function of exciton energy.** Top panel: Polarization-averaged oscillator strength as a function of the corresponding exciton energy. Dashed, vertical lines highlight the positions of the first four optically active excitons. Middle and bottom panel: Phonon branch-averaged exciton-phonon coupling as a function of the corresponding exciton energy, summed over final exciton states (middle panel) or diagonal matrix elements only (bottom panel). Dashed, vertical lines as in the top panel.

In Fig. S3, we show the oscillator strength (top panel) and the exciton-phonon coupling (middle and bottom panels). We use the term *oscillator strength* to refer to the in-plane polarization-averaged quantity $|d_S|^2 \equiv \sum_{\mu} |d_S^{\mu}|^2/2$, with d_S^{μ} having been defined in Eq. (4) of the main text. The exciton spectrum features four strongly optically active states with energies $E_S = 5.541$ eV, 5.878 eV, 6.085 eV, and 6.312 eV, each of which is doubly degenerate due to inversion symmetry. In Fig. S3, these *bright* states are highlighted by dashed, vertical lines.

To visualize the exciton-phonon coupling, we look at the exciton-phonon coupling averaged over the two degenerate, in-plane, Raman-active phonon branches: $\sum_{\lambda} |g_{S,S'}^{\lambda}|^2/2$, where $g_{S,S'}^{\lambda}$ was defined in Eq. (5) of the main text. We look at both the final state-summed matrix elements and the diagonal parts only.

By comparing the two, it becomes clear that intra-exciton scattering plays almost no role for the degenerate optical phonon in the regime of the dominant first four bright excitons. This is entirely in accordance with parity conservation, which forbids a coupling of the same excitonic state via the degenerate optical in-plane phonon, which has odd parity. As such, the main contribution to the Raman process comes from parity-flipping, inter-exciton scattering within the same doublet.

Excitonic envelope wave functions

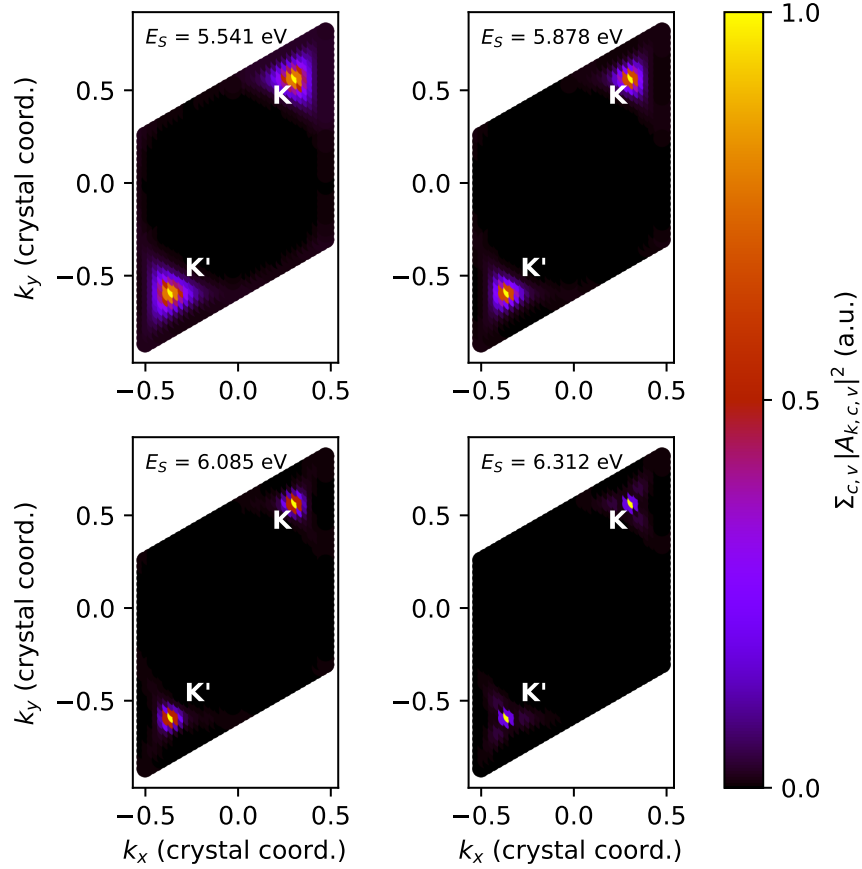


FIG. S4. hBN: Exciton envelope wave functions in reciprocal space.

Each panel shows the band-summed square of the envelope wave function $|A_{\mathbf{k},c,v}^S|^2$ as a function of wave vector \mathbf{k} in the plane containing the Γ - and K -point. Shown are the wave functions of the the first four bright excitons as highlighted by vertical lines in Fig. S3.

In Fig. S4, we show the state-summed envelope wave functions for the first four bright excitons as a function of wave vector \mathbf{k} in the plane containing the Γ - and K -point (compare also Ref. [7] for the single-layer case). While the first bright exciton is strongly delocalized in \mathbf{k} -space, the second one is already more localized around the K - and K' -points, although still showing a trigonally warped shape. By contrast, the third and fourth excitons are strongly localized around $K^{(\prime)}$ and their wave functions are circularly symmetric. Together with the circularly symmetric band structure around the $K^{(\prime)}$ -point, this leads to the system behaving as if it featured almost full rotation symmetry and hence resonant Raman scattering involving a degenerate phonon mode is suppressed on account of angular momentum conservation [8–10].

S3. SUPPLEMENTARY INFORMATION FOR THE MOS_2 CALCULATION

Here we provide more information computational details for the calculations for monolayer molybdenum disulfide. In addition, we show the electronic band structure and the exciton spectrum, including the exciton oscillator strength and the exciton-phonon coupling. Lastly, we provide a plot of the excitonic envelope wave functions in reciprocal space for the first three optically active excitons.

Computational details

The ground state properties of monolayer molybdenum disulfide were computed on the level of density functional theory within the local density approximation for the exchange-correlation functional in the parametrization due to Perdew and Zunger [2]. All DFT calculations were performed with the `PWscf` code of the `QuantumESPRESSO` suite [3] using norm-conserving, fully relativistic pseudopotentials for both sulfur and molybdenum to account for the effects of spin-orbit interactions. We use a plane-wave basis set with an energy cutoff of 90 Ry for the electronic wave functions and 360 Ry for the charge density. For integrations over the first Brillouin zone, a uniform \mathbf{k} -point mesh of size $12 \times 12 \times 1$ was used. The lattice parameter was relaxed prior to the calculation, yielding a value of $a=3.170$ Å for the in-plane lattice constant. To preserve the single-layer nature of the system, we use a vacuum spacing of 16 Å between periodic images of the monolayer. For the electronic excited state properties, we computed the electronic band structure on a $24 \times 24 \times 1$ \mathbf{k} -point mesh with spin-orbit coupling for 400 (in general spin-non-degenerate) bands.

The calculation of the excitonic eigenenergies and envelope wave functions was performed with the `yambo` code [4]. The two-particle interaction kernel was computed on the level of the Tamm-Dancoff approximation as the sum of a statically screened attractive Coulomb part plus a repulsive bare exchange part. The static inverse dielectric screening function was computed on the level of the random phase approximation using plane-wave cutoffs of 60 Ry each for the electronic wave functions and the dielectric response function in reciprocal space. For the calculation of the actual two-particle interaction kernel, we truncated the attractive screened Coulomb part at a plane-wave energy cutoff of 10 Ry and the repulsive bare exchange part at a plane-wave cutoff of 20 Ry. We included the upper eight valence and lower eight conduction bands in the construction of the two-particle interaction kernel. A rigid band shift of 0.925 eV was added to all independent-particle transition energies in order to account for the underestimation of the band gap in DFT. This value was obtained in previous first principle calculations on the level of the GW approximation [11]. Finally, we solve the Bethe-Salpeter equation iteratively for the first 2000 excitonic eigenenergies and envelope wave functions using the `SLEPc` library [6].

For the screened electron-phonon coupling, we approximate the two-particle interaction kernel on the level of time-dependent density functional theory. As this approximation is equivalent to obtaining the screened electron-phonon matrix elements with density functional perturbation theory [1], we calculate the screened matrix elements with the `PH` code of the `QuantumESPRESSO` suite [3]. Lastly, for the phonon frequencies of the degenerate, Raman-active in-plane optical mode of E' -symmetry and the non-degenerate out-of-plane mode of A'_1 -symmetry, we use the previously calculated values of 391.7 cm^{-1} and 410.3 cm^{-1} [12].

Electronic band structure

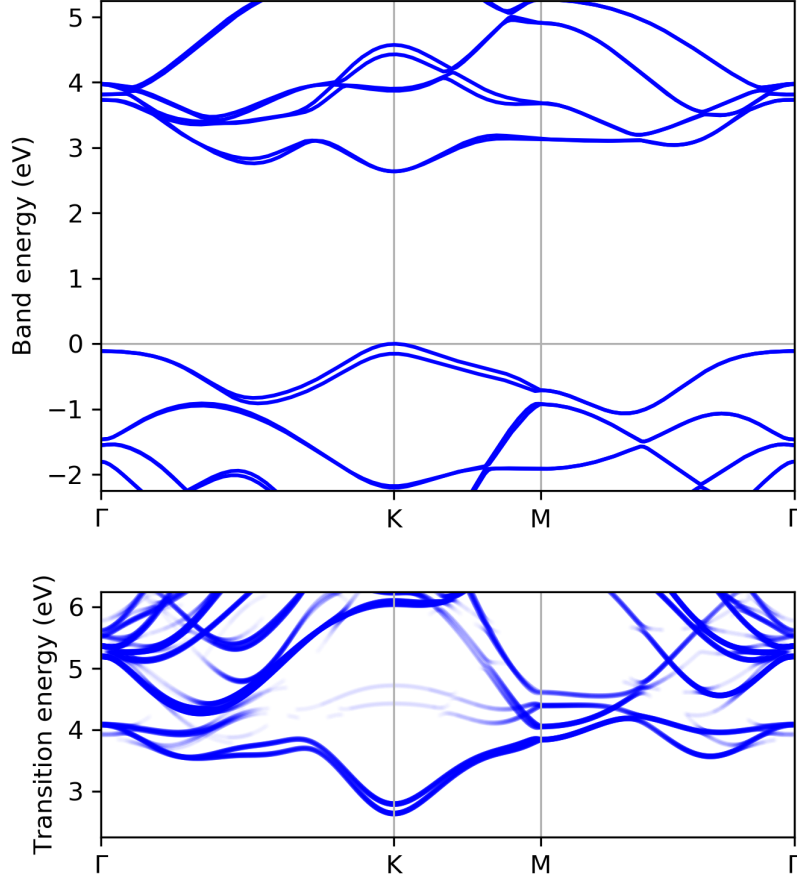


FIG. S5. **MoS₂: Electronic (transition) band structure.** Top: Electronic band structure on the level of Kohn-Sham DFT within the LDA. A rigid shift of 0.925 eV was added to all conduction band energies. Bottom: Electronic transition band structure obtained from the electronic band structure. The opacity of the lines corresponds to the optical activity of the transition.

The electronic band structure of monolayer molybdenum disulfide is shown in Fig. S5. Again we show both the electronic band structure on the level of Kohn-Sham density functional theory on the level of the local density approximation (left panel) and the resulting transition band structure (right panel). As mentioned in the previous section, we shifted all conduction bands by 0.925 eV to account for the underestimation of the band gap in DFT [11].

The band structure is characterized by a direct gap of 2.633 eV at the K -point. The top of the valence band features a spin-orbit coupling-induced splitting of 0.112 eV, as its orbital decomposition involves Mo d -orbitals with finite angular momentum in z -direction, i.e., spin direction. By contrast, the conduction band bottom features a much smaller spin-orbit coupling-induced splitting of 0.003 eV, as it is mostly composed of Mo d -orbitals with zero angular momentum in z -direction. As a result the low-energy transition band structure consists of two almost degenerate doublets of transitions, separated by the valence band spin-orbit coupling-induced splitting. Due to the strong spin-orbit coupling, each member of the almost degenerate doublet is spin polarized. As a result, only one member of each doublet is optically active as a photon cannot flip the spin.

Finally, and as in the case of hBN, the transition band structure around the K -point is fully rotationally symmetric. This is important for the physics of Raman scattering involving the lower two excitons, which receive finite contributions only from the region around the $K^{(l)}$ -point. As mentioned in the main text, this suppresses Raman scattering involving a finite angular momentum phonon, as in the case of the E' -mode in the low-energy regime (compare also the case of MoTe₂ [10]).

Exciton spectrum: Oscillator strength and exciton-phonon coupling

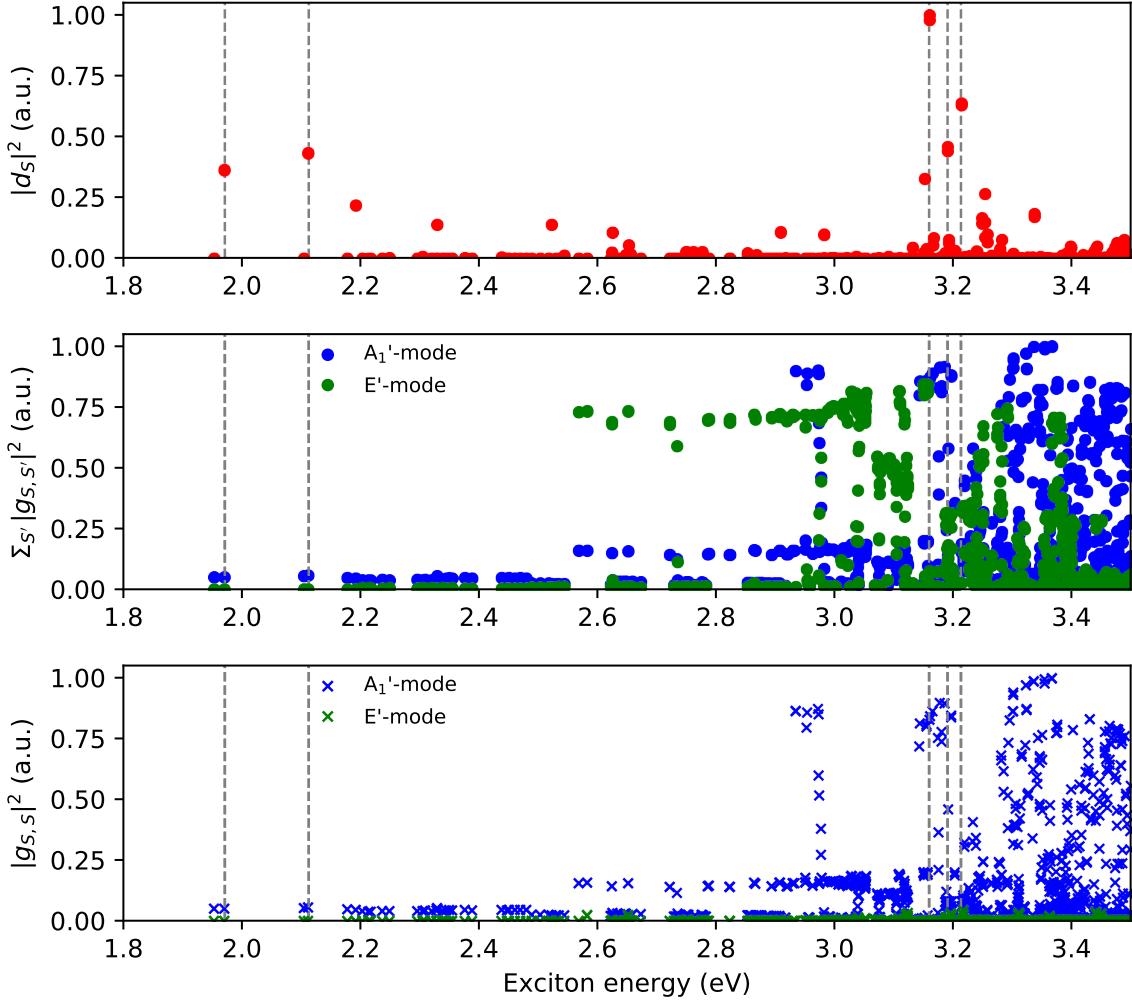


FIG. S6. **MoS₂: Oscillator strength and exciton-phonon coupling as a function of exciton energy.** Top panel: Polarization-averaged oscillator strength as a function of the corresponding exciton energy. Dashed, vertical lines highlight the positions of the “A”-, “B”-, and “C”-excitons. Middle and bottom panel: Exciton-phonon coupling as a function of the corresponding exciton energy, summed over final exciton states (middle panel) or diagonal matrix elements only (bottom panel). Green symbols represent the branch-averaged exciton-phonon coupling for the degenerate, in-plane E' -mode. Blue symbols represent the coupling to the out-of-plane A_1' -mode. Dashed, vertical lines as in the top panel.

In Fig. S6, we show the oscillator strength (top panel) and the exciton-phonon coupling (middle and bottom panels). As before, we use the term *oscillator strength* to refer to the in-plane polarization-averaged quantity $|d_S|^2 \equiv \sum_{\mu} |d_S^{\mu}|^2/2$, with d_S^{μ} having been defined in Eq. (4) of the main text. The exciton spectrum features three strongly optically active states with energies $E_S = 1.971$ eV, 2.113 eV, and 3.160 eV, each of which is doubly degenerate due to horizontal mirror plane symmetry. In line with the recent literature (e.g. Ref. [13]), we refer to these excitonic states as the “A”-, “B”-, and “C”-excitons, respectively. In Fig. S6, these *bright* states are highlighted by dashed, vertical lines.

To visualize the exciton-phonon coupling, we look at the exciton-phonon coupling for the in-plane E' -mode (green symbols) and the out-of-plane A_1' -mode (blue symbols), separately. As in the case of hBN, we average over the two degenerate Raman-active in-plane phonon branches of the E' -mode: $\sum_{\lambda} |g_{S,S'}^{\lambda}|^2/2$, where $g_{S,S'}^{\lambda}$ was defined in Eq. (5) of the main text. Again, we look at both the final-state summed matrix elements and the diagonal parts only.

Contrary to the case of hBN, here, the exciton-phonon coupling in the low-energy regime is dominated by intra-exciton scattering. This can be attributed to the horizontal mirror plane symmetry, under which the phonon transforms evenly and which hence forbids a coupling between two excitons of different mirror parity.

as would be the case for inter-exciton scattering within the same doublet. In addition to this, in the low-energy regime, the excitonic states are energetically well-separated and thus the overlap between the envelope wave functions of successive excitons of the same mirror parity is small, i.e., inter-doublet scattering is also suppressed. Note also that the exciton envelope wave functions are circularly symmetric in this regime, i.e., the low-energy excitons can be assigned a definite angular momentum of $\pm\hbar$. As a result, their intra-exciton coupling via the E' -mode of angular momentum $\pm\hbar$ is forbidden on account of angular momentum conservation, i.e., the E' -mode is silent in Raman scattering in the low-energy regime.

When the higher-energy exciton continuum is entered, the in- and out-of-plane mode couplings start to behave differently, however. In case of the E' -mode, inter-exciton scattering becomes dominant, due to the fact that the exciton continuum is dominated by excitons with delocalized and trigonally warped envelope wave functions (see, for instance the last panel of Fig. S7). Hence, not all inter-exciton couplings are suppressed by symmetry anymore. For the out-of-plane A'_1 -mode, on the other hand, the situation is still the same, as it, due to its scalar nature, can still only mediate intra-exciton scattering.

Excitonic envelope wave functions

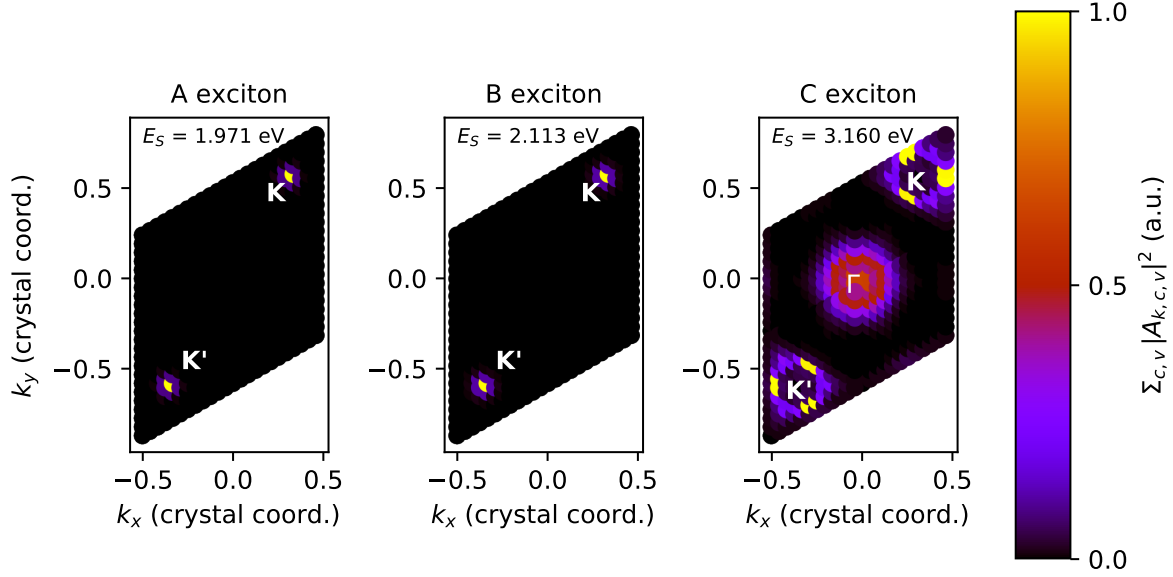


FIG. S7. **MoS₂: Exciton envelope wave functions in reciprocal space.**

Each panel shows the band-summed square of the envelope wave function $|A_{\mathbf{k},c,v}^S|^2$ as a function of wave vector \mathbf{k} . Shown are the wave functions of the first three bright excitons (the “A”-, “B”-, and “C”-excitons), which are also highlighted by vertical lines in Fig. S6.

In Fig. S7, we show the state-summed envelope wave functions for the first three bright excitons, the so-called “A”-, “B”-, and “C”-excitons, as a function of wave vector \mathbf{k} . Both the “A”- and “B”-exciton are strongly localized around the K - and K' -point. In band space, they are dominated by transitions from the valence band bottom to the conduction band top, with the spin-orbit splitting of the valence band corresponding to the energy difference of the “A”- and “B”-exciton. By contrast, the “C”-exciton can no longer be attributed to a single, localized transition, but instead receives contributions from across large parts of the first Brillouin zone. As in the case of hBN, the circularly symmetric shape of the envelope wave functions of the “A”- and “B”-excitons means that in the corresponding energy regime, Raman scattering involving the degenerate in-plane E' -mode is suppressed due to angular momentum conservation [8–10]. By contrast, Raman scattering involving the A_1' -mode is still allowed as the latter does not carry any angular momentum. For the “C”-exciton, by contrast, the envelope wave function is strongly trigonally warped and hence both Raman modes are visible in the Raman spectrum.

-
- [1] S. Reichardt, *Many-Body Perturbation Theory Approach to Raman Spectroscopy and Its Application to 2D Materials*, Ph.D. thesis, RWTH Aachen University & University of Luxembourg (2018).
 - [2] J. P. Perdew and A. Zunger, *Phys. Rev. B* **23**, 5048 (1981).
 - [3] P. Giannozzi, S. Baroni, N. Bonini, M. Calandra, R. Car, C. Cavazzoni, D. Ceresoli, G. L. Chiarotti, M. Cococcioni, I. Dabo, A. Dal Corso, S. de Gironcoli, S. Fabris, G. Fratesi, R. Gebauer, U. Gerstmann, C. Gougoussis, A. Kokalj, M. Lazzeri, L. Martin-Samos, N. Marzari, F. Mauri, R. Mazzarello, S. Paolini, A. Pasquarello, L. Paulatto, C. Sbraccia, S. Scandolo, G. Sclauzero, A. P. Seitsonen, A. Smogunov, P. Umari, and R. M. Wentzcovitch, *J. Phys. Condens. Matter* **21**, 395502 (2009).
 - [4] A. Marini, C. Hogan, M. Grüning, and D. Varsano, *Comput. Phys. Commun.* **180**, 1392 (2009).
 - [5] B. Arnaud, S. Lebègue, P. Rabiller, and M. Alouani, *Phys. Rev. Lett.* **96**, 026402 (2006).
 - [6] V. Hernandez, J. E. Roman, and V. Vidal, *ACM Trans. Math. Softw.* **31**, 351 (2005).
 - [7] T. Galvani, F. Paleari, H. P. C. Miranda, A. Molina-Sánchez, L. Wirtz, S. Latil, H. Amara, and F. Ducastelle, *Phys. Rev. B* **94**, 125303 (2016).
 - [8] S. Reichardt and L. Wirtz, in *Optical Properties of Graphene*, edited by R. Binder (World Scientific, Singapore, 2017) Chap. 3, pp. 85–132.
 - [9] S. Reichardt and L. Wirtz, *Phys. Rev. B* **95**, 195422 (2017).
 - [10] H. P. C. Miranda, S. Reichardt, G. Froehlicher, A. Molina-Sánchez, S. Berciaud, and L. Wirtz, *Nano Lett.* **17**, 2381 (2017).
 - [11] A. Molina-Sánchez, M. Palummo, A. Marini, and L. Wirtz, *Phys. Rev. B* **93**, 155435 (2016).
 - [12] A. Molina-Sánchez and L. Wirtz, *Phys. Rev. B* **84**, 155413 (2011).

- [13] A. Molina-Sánchez, D. Sangalli, K. Hummer, A. Marini, and L. Wirtz, *Phys. Rev. B* **88**, 045412 (2013).